Monthly Notices of the ROYAL ASTRONOMICAL SOCIETY

MNRAS **528,** 4941–4957 (2024) https://doi.org/10.1093/mnras/stae294
Advance Access publication 2024 January 27

ω Centauri: a MUSE discovery of a counter-rotating core

Renuka Pechetti [1]★ Sebastian Kamann [1]★ Davor Krajnović,[2]★ Anil Seth,[3] Glenn van de Ven [4] Nadine Neumayer,[5] Stefan Dreizler,[6] Peter M. Weilbacher,[2] Sven Martens[6] and Florence Wragg [1]

[1]*Liverpool John Moores University, Astrophysics Research Institute, Liverpool, L3 5RF, UK*
[2]*Leibniz–Institut für Astrophysik Potsdam (AIP), Postdam, 14482, Germany*
[3]*University of Utah,Department of Physics and Astronomy, Salt Lake City, Utah, 84112,USA*
[4]*University of Vienna, Department of Astrophysics,Vienna,1180, Austria*
[5]*Max Planck Institut für Astronomie, Heidelberg, 69117, Germany*
[6]*Institut für Astrophysik, Göttingen, 37077, Germany*

Accepted 2024 January 19. Received 2023 December 9; in original form 2023 April 20

ABSTRACT

ω Centauri is considered the most massive globular cluster of the Milky Way and likely the former nuclear star cluster of a Galaxy accreted by the Milky Way. It is speculated to contain an intermediate-mass black hole (IMBH) from several dynamical models. However, uncertainties regarding the location of the cluster centre or the retention of stellar remnants limit the robustness of the IMBH detections reported so far. In this paper, we derive and study the stellar kinematics from the highest-resolution spectroscopic data yet, using the Multi Unit Spectroscopic Explorer (MUSE) in the narrow field mode and wide field mode. Our exceptional data near the centre reveal for the first time that stars within the inner 20 arcsec ($\sim$0.5 pc) counter-rotate relative to the bulk rotation of the cluster. Using this data set, we measure the rotation and line-of-sight velocity dispersion profile out to 120 arcsec with different centres proposed in the literature. We find that the velocity dispersion profiles using different centres match well with those previously published. Based on the counter–rotation, we determine a kinematic centre and look for any signs of an IMBH using the high-velocity stars close to the centre. We do not find any significant outliers >60 km s^{-1} within the central 20 arcsec, consistent with no IMBH being present at the centre of ω Centauri. A detailed analysis of Jeans' modelling of the putative IMBH will be presented in the next paper of the series.

Key words: stars: kinematics and dynamics – (Galaxy:) globular clusters: individual – galaxies: star clusters: general – galaxies: star clusters: individual.

1 INTRODUCTION

The most massive cluster of the Milky Way, ω Centauri (NGC 5139), has been a topic of discussion for more than four decades now (e.g. Freeman & Rodgers 1975; Geyer, Hopp & Nelles 1983; Meylan et al. 1995; Lee et al. 2002). Many studies have also theorized that it might be the surviving nucleus (or nuclear star cluster, NSC) of a stripped dwarf Galaxy due to the presence of complex stellar populations that display a broad metallicity distribution (e.g. Johnson & Pilachowski 2010; Husser et al. 2020), and are far more complex than the multiple populations routinely found in other clusters (e.g. Gratton, Carretta & Bragaglia 2012; Piotto et al. 2015; Martocchia et al. 2018). It also has evidence for a central stellar disk and tangential velocity anisotropy consistent with tidal stripping (e.g. van de Ven et al. 2006). More recently, data from the Gaia satellite was used to trace the origin of Galactic globular clusters (GCs; Massari, Koppelman & Helmi 2019), and ω Centauri was suggested to be the former core of the *Gaia*-Enceladus/Sausage galaxy (Forbes 2020; Pfeffer et al. 2021), which was a dwarf galaxy with a mass of $\sim 10^8$ M$_\odot$ accreted by the Milky Way $\sim$10 Gyr ago (Helmi et al. 2018).

Several stripped nuclei, sometimes known as ultra-compact dwarf galaxies (UCDs), were recently detected around nearby galaxies. These remnants of more massive galaxies ($>10^9$ M$_\odot$) are capable of hosting supermassive black holes with masses $>10^6$ M$_\odot$ (e.g. Seth et al. 2014; Ahn et al. 2017, 2018). Recent analyses have further shown that somewhat less massive black holes (BHs) are present in all five of the nearest early-type galaxies with stellar masses $\sim 10^9$ M$_\odot$ and NSC masses between 2×10^6–7×10^7 M$_\odot$ (Nguyen et al. 2017, 2018, 2019). Therefore, one might expect a high fraction of stripped NSCs from this mass range of galaxies to also host massive BHs $<10^6$ M$_\odot$. Indeed, a 10^5 M$_\odot$ BH was recently found in the M31 GC, B023-G078 (Pechetti et al. 2022). Like ω Centauri, this object has additional evidence of being a stripped nucleus. There have been other proposed detections, for example, G1 in M31 (Gebhardt, Rich & Ho 2005), M54 (Ibata et al. 2009), the likely nuclear star cluster of the Sagittarius dwarf galaxy (e.g. Alfaro-Cuello et al. 2019). This establishes that GCs are potential sites of IMBHs despite the lack of robust detections in Milky Way GCs. Completing our picture of the number density of massive BHs in the cosmic neighbourhood is a crucial step towards understanding the formation of the seed BHs in the early Universe (e.g. Volonteri

★ E-mail: r.pechetti@ljmu.ac.uk (RP);S.Kamann@ljmu.ac.uk (SK);dkrajnovic@aip.de (DK)

2010; Greene, Strader & Ho 2020) as well as the correlations between galaxies and their BHs (e.g. Saglia et al. 2016; Habouzit et al. 2021).

ω Centauri is a perfect candidate to search for an IMBH since it is the most massive cluster in the Milky Way, with a dynamical mass of 2.5–3.5 $\times$ 10^6 $M_\odot$ (van de Ven et al. 2006; Baumgardt & Hilker 2018), and an outlier in the globular cluster luminosity function (Kruijssen & Portegies Zwart 2009). Like M54, it is an outlier from regular globular clusters in the relation between average metallicity and intrinsic metallicity spread (e.g. fig. 2 of Leaman (2012)), where both lie on the dwarf galaxy sequence. It is strongly rotating with a rotation velocity of $\sim$4–5 km s^{-1} (Meylan & Mayor 1986; Merritt, Meylan & Mayor 1997; Sollima, Baumgardt & Hilker 2019) and has one of the highest central velocity dispersions of $\sim$22 km s^{-1} (Noyola et al. 2010), which makes it an outlier in the V/σ among the Galactic GCs. The rise in the velocity dispersion in (Noyola et al. 2010) suggests the presence of an IMBH, but an IMBH is not the only solution. Several analyses, such as Baumgardt et al. (2019) and Zocchi, Gieles & Hénault-Brunet (2019) have shown that this rise could also be caused by the presence of an extended mass distribution consisting of stellar-mass BHs instead of a single IMBH. Zocchi, Gieles & Hénault-Brunet (2019) further show that if radial anisotropy near the centre is considered, a central extended dark mass of <5 per cent of the cluster mass is sufficient to explain the observed kinematics. Other studies have also proposed the possibility of concentrated non-baryonic matter present in the core of ω Centauri. For example, assuming a Navarro–Frenk–White (NFW) profile, Brown et al. (2019) find an integrated dark mass of $\sim$5 $\times$ 10^5 $M_\odot$ at the cluster centre. Evans, Strigari & Zivick (2022) performed an analysis with different dark matter profiles for the central dark mass in the cluster and found that although stellar remnants can explain masses <5 $\times$ 10^5 $M_\odot$, any mass greater than that cannot be explained by it. Although various interpretations can be given for the central dark mass component, no conclusions have been found robustly yet.

A major source of uncertainty in dynamical measurements are the central density slope and the velocity dispersion profile, which changes based on the adopted centre of the cluster, of which several estimates exist from Noyola, Gebhardt & Bergmann (2008), Noyola et al. (2010), and van der Marel & Anderson (2010), which are hereafter referred to as NGB08, N10, and vdMA10, respectively. These studies estimate centres based on kinematics or photometry and from different data sets such as integrated kinematics and proper motions of the stars. The NGB08 centre was determined based on the central density of ω Centauri and is $\sim$12 arcsec away from N10 and vdMA10 centre. The N10 and vdMA10 centres are $\sim$3 arcsec apart but were determined using kinematics and number density counts, respectively. These centres have produced different dispersion profiles, for example, the profile in N10 peaks strongly resulting in a central velocity dispersion of $\sim$22 km s^{-1} whereas the dispersion profile of vdMA10 is relatively flatter at $\sim$ 19 km s^{-1} towards the centre. This has also resulted in different estimates for the IMBH mass where NGB08 and N10 argued for the presence of an IMBH with a mass of 4–5 $\times$ 10^4 $M_\odot$, whereas vdMA10 found that no IMBH was required to fit the observed kinematics of the cluster. As noted by vdMA10 and N10, the exact location of the centre along with the kinematics based on that centre are necessary for arguing the presence of an IMBH.

A detailed analysis of the kinematics is thus required to solve the discrepancies regarding the centre. With ω Centauri being the most extensively studied cluster in the Milky Way, several kinematic data sets from different instruments exist. We have obtained the highest spatial resolution data (50 mas) yet in the central 20 arcsec using integrated field MUSE-NFM spectroscopy. We also obtained MUSE-WFM spectroscopy for $\sim$40 000 stars within the half-light radius of this cluster to quantify the presence of a dark mass, either in the form of an IMBH (Noyola et al. 2010; Baumgardt 2017) or a collection of stellar mass BHs that have mass segregated to the central regions of the cluster (Baumgardt et al. 2019; Zocchi, Gieles & Hénault-Brunet 2019). We revisit two crucial aspects in this paper that are required to probe the presence (and constrain the potential mass) of an IMBH in ω Centauri, namely the central kinematics as well as the determination of the cluster centre. The latter will also enable an accurate determination of the surface brightness profile. We analyse the kinematics based on the different existing centres proposed in the literature and attempt to determine the kinematic centre based on the detection of a centralized rotation signal. In a subsequent paper, an analysis of the presence/absence of the IMBH is done based on the Jeans' modelling of the kinematics.

This paper is organized as follows. In Section 2 we present the imaging and spectroscopic data. Section 3 presents the analysis of the kinematic data based on the different centres and Section 4 describes the analysis of the inner 20 arcsec of the cluster. Section 5 consists of a discussion on the existence of high-velocity stars in ω Centauri. Section 6 contains our summary and conclusions.

2 MUSE DATA – OBSERVATION AND REDUCTION

The observations used in this paper were carried out as a part of MUSE guaranteed time observations (GTO) of 25 GCs (PIs: S. Kamann and S. Dreizler). We selected the clusters to be within 15 kpc and have central velocity dispersions of >5 km s^{-1}. They were observed during multiple epochs, enabling binary stars to be detected. An overview of the survey is provided in Kamann et al. (2018). Another survey was also carried out using the MUSE-General Observer (GO) program, 105.20CG.001 (PI: N. Neumayer) and published in Nitschai et al. (2023), which contains the catalogue with a combination of the GO data and our GTO data. For the analysis of ω Centauri here, we only used a combination of wide field mode (WFM) and narrow field mode (NFM) GTO observations.

The WFM observations consist of the data presented in Latour et al. (2021) plus three additional epochs of observations taken during the nights 2021-05-09, 2021-08-05, and 2022-05-29 as part of program 105.20CR and 109.23DV. In total, 10 WFM pointings of 1 $\times$ 1 arcmin each have been observed for 15 epochs on average. To this data set, we add NFM observations consisting of 6 pointings of size 7.5 arcsec $\times$ 7.5 arcsec, observed during 6 nights (2019-04-06, 2019-05-03, 2020-02-23, 2021-05-09, and 2022-05-29) as part of observing programs 0103.D-0204, 0104.D-0257, 105.20CR, and 109.23DV. An overview of the different pointings used in this work, including their number of epochs, total exposure times, and median seeing values, is provided in Table 1. The location of NFM pointings 91 to 94 was chosen to cover the different centres of ω Centauri that have been proposed in the literature (NGB08, N10, vdMA10), while pointings 98 and 99 resulted from a misidentification of the requested tip-tilt star at the telescope. VRI mosaics created from the reduced WFM and NFM data are shown in Fig. 1. The NFM data span $\sim$20 arcsec $\times$ 15 arcsec, while the WFM data span approximately 3 arcmin $\times$ 5 arcmin other than the two pointings that are $\sim$5 arcmin away from the centre. These pointings were observed to complete the radial coverage inside the half-light radius of the cluster.

The raw data were reduced using the standard MUSE pipeline (Weilbacher et al. 2020) in versions 1.2 and later. All NFM data were reduced with pipeline version 2.8, which includes a strongly

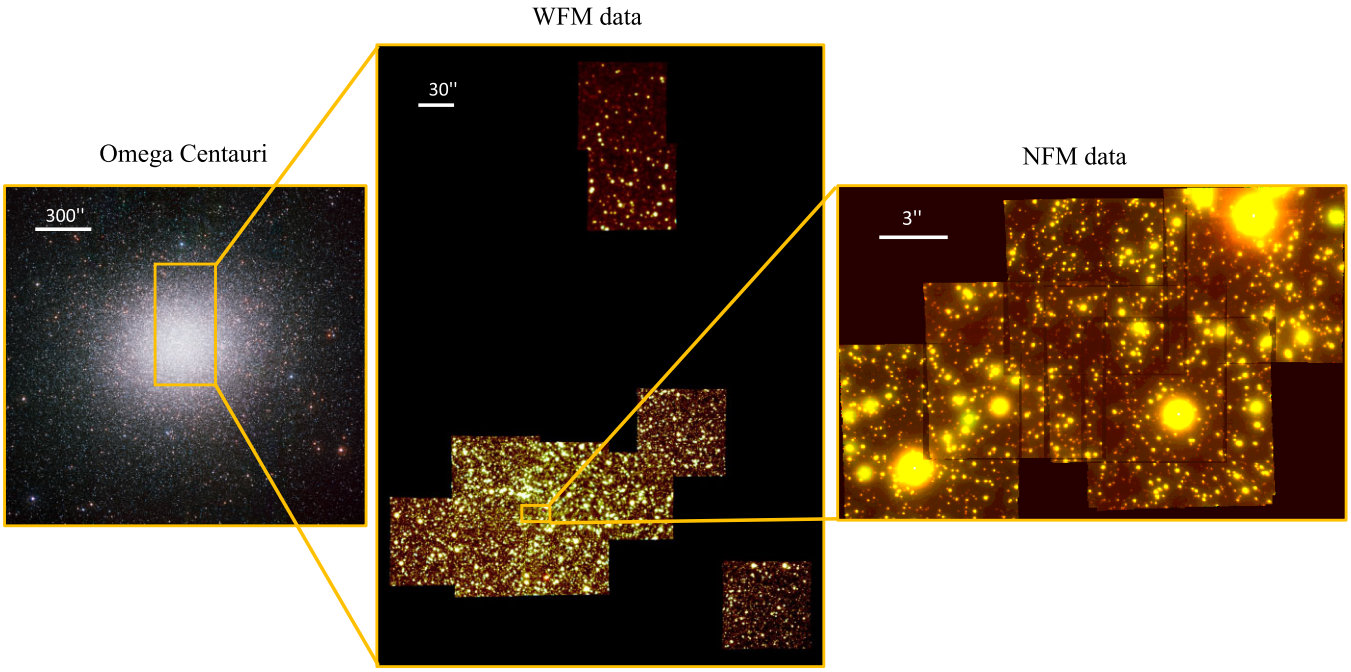

Figure 1. Multi Unit Spectroscopic Explorer (MUSE) data of ω Centauri. The left panel shows a 0.5° image of ω Centauri (image credit: ESO, https://www.eso.org/public/images/eso0844a/). The wide field mode (WFM) data in the middle panel consists of 10 pointings of 1 arcmin × 1 arcmin each that were repeatedly observed for at least >12 epochs. Two of the pointings were taken ∼5 arcmin away from the cluster centre to cover the half-light radius of the cluster. The right panel shows the narrow field mode (NFM) data which span ∼20 arcsec × 15 arcsec of which each pointing has a size of 7.5 arcsec × 7.5 arcsec.

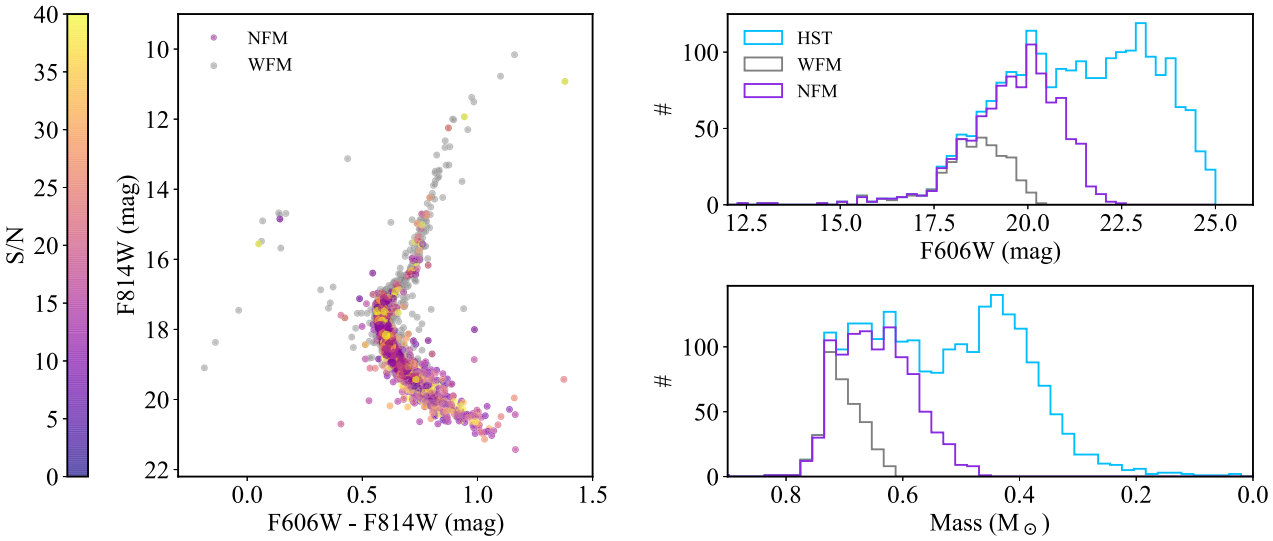

Figure 2. Left: Colour–magnitude diagram of ω Centauri. The points are the 963 NFM (coloured) and 1552 WFM (grey) stars within 20 arcsec from the van der Marel & Anderson (2010) centre. They are coloured by the S/N of the spectrum as determined during the extraction of the MUSE spectra. Right: Completeness histogram of MUSE NFM and WFM data as a function of magnitude and stellar mass on the NFM footprint. Grey lines correspond to the WFM data and the solid purple lines represent NFM data. The NFM data goes 2 mag deeper than the WFM data and extends beyond 20 mag in the F625W band within 20 arcsec from the centre. The mass range of the stars covered by the NFM is also broader with stellar masses starting from ∼0.5 $M_\odot$.

improved NFM flux calibration compared to the previous versions. We used the default settings of the pipeline, with two exceptions. First, we did not perform a sky subtraction, as it would also remove stellar light given the crowding of the observed fields. Second, we did not perform a correction for telluric absorption, which instead was corrected during the analysis of the spectra (see below). Data cubes were created for individual pointings and epochs, and they typically combined three (for WFM observations) or four (for NFM)

Table 1. MUSE observations analysed in this work summarized per pointing.

Pointing no.	Mode	RA	Dec	N_{epochs}	$N_{exposures}$ [s]	Total exp. time [arcsec]	Median seeing
Pointing 01	WFM	13:26:45.0	−47:29:09	15	45	2025	0.62
Pointing 02	WFM	13:26:45.0	−47:28:24	14	42	1890	0.61
Pointing 03	WFM	13:26:49.5	−47:29:09	17	51	2253	0.60
Pointing 04	WFM	13:26:49.5	−47:28:24	17	51	2295	0.62
Pointing 05	WFM	13:26:40.6	−47:28:31	14	46	3646	0.60
Pointing 06	WFM	13:26:53.9	−47:29:01	17	51	4080	0.62
Pointing 07	WFM	13:26:36.8	−47:27:54	15	45	4500	0.60
Pointing 08	WFM	13:26:31.0	−47:29:55	16	49	7350	0.62
Pointing 11	WFM	13:26:40.3	−47:25:00	14	43	12 900	0.92
Pointing 12	WFM	13:26:41.0	−47:24:03	12	36	21 600	0.82
Pointing 91	NFM	13:26:47.2	−47:28:50	2	8	4800	0.08
Pointing 92	NFM	13:26:46.1	−47:28:45	2	8	4800	0.08
Pointing 93	NFM	13:26:46.8	−47:28:46	3	11	6080	0.06
Pointing 94	NFM	13:26:46.5	−47:28:51	2	8	4800	0.07
Pointing 98	NFM	13:26:46.6	−47:28:49	1	4	2400	0.08
Pointing 99	NFM	13:26:47.5	−47:28:51	1	4	2400	0.07

exposures. In between exposures, derotator offsets of 90° and small spatial dithers were applied.

The reduced data cubes were processed using PAMPELMUSE (Kamann, Wisotzki & Roth 2013; Kamann 2018), which performs a deblending of the individual stellar spectra based on a wavelength-dependent model of the point spread function (PSF) that is recovered from the data and a wavelength-dependent coordinate transformation from a reference source catalogue to the MUSE data. As reference catalogues for ω Centauri, two publicly available *Hubble Space Telescope* (*HST*) data sets were used. The central WFM pointings (01–05, cf. Table 1), as well as all NFM pointings used the catalogue created by Anderson et al. (2008) for the ACS survey of Galactic GCs (Sarajedini et al. 2007). The outer WFM pointings (06–12), which are not or only partially covered by the ACS footprint, used the photometric catalogue generated by Anderson & van der Marel (2010). As a PSF model, we used a Moffat profile for all WFM cubes and optimized the FWHM as well as the kurtosis (parametrized by β, cf. Kamann, Wisotzki & Roth 2013) as a function of wavelength. In cases where visual inspection of the cubes suggested elongated stars, we included the ellipticity and the position angle (PA) of the semi-major axis of the Moffat in the set of free parameters. While the Moffat profile has been shown to accurately describe the WFM-PSF (Fusco et al. 2020), it cannot describe the more complicated shape of the NFM-PSF. Hence, the NFM data were instead processed using the MAOPPY model developed by Fétick et al. (2019), which has previously been successfully applied to NFM observations of the Galactic globular cluster M80 (NGC 6093) by Göttgens et al. (2021).

The extracted spectra were processed in several analyses to measure the line-of-sight (LOS) velocities and determine the stellar parameters of the corresponding stars. These analyses rely on useful initial guesses, which we obtained by comparing the aforementioned photometric catalogues to isochrones from the data base of Bressan et al. (2012), where we assumed an age of 13 Gyr, a metallicity of [Fe/H] $= -1.33$, and an extinction of $A_V = 0.37$. Initial guesses for the surface temperature $\log g$ and the effective temperature $T_{\rm eff}$ of each star were obtained by finding the point that is closest to the isochrone in a colour–magnitude diagram (CMD). An $m_{\rm F606W} - m_{\rm F814W}$ versus $m_{\rm F606W}$ CMD was used for the Anderson et al. (2008) catalogue, while an $m_{\rm F435W} - m_{\rm F625W}$ versus $m_{\rm F625W}$ CMD was used for the Anderson & van der Marel (2010) photometry. Note that despite the strong evidence for metallicity and/or age variations within ω Centauri, we only used a single isochrone when deriving initial parameter guesses. This is because all parameters except for $\log g$ were later refined during the spectral analysis. $\log g$ was not refined because it impacts the shapes of the spectral lines rather than their strengths, and thus is difficult to measure at the low spectral resolution of MUSE. Moreover, $\log g$ is only weakly dependent on the age and metallicity of the old stars present in the cluster. To infer LOS velocities, we first cross–correlated each extracted spectrum against various templates drawn from the PHOENIX spectral library presented in Husser et al. (2013). The templates were chosen to represent the range in stellar parameters expected in ω Centauri ($T_{\rm eff} = \{3\,000\ {\rm K}, 6\,000\ {\rm K}, 9\,000\ {\rm K}\}$, $\log g = \{1, 3, 5\}$), but had solar metallicity. We selected the LOS velocity provided by the template that gave the strongest cross-correlation signal and used it as an initial guess for the following full-spectrum fit with SPEXXY (Husser et al. 2016). When reliable initial guesses could not be obtained from the cross–correlation, the spectra were then initialized at the systemic velocity of ω Centauri. During the full spectrum fit, which was performed using templates from the PHOENIX library of Husser et al. (2013), we determined [Fe/H] and $T_{\rm eff}$ alongside the LOS velocity. As illustrated in Husser et al. (2016), SPEXXY enables the user to fit the telluric absorption simultaneously with the stellar spectrum, which was done while analysing the spectra. To verify the wavelength accuracy of every MUSE cube, we determined the average velocity of the telluric absorption fits of all spectra extracted with an S/N > 30. This mean telluric velocity, which usually varied between -1 and $1\,{\rm km\,s^{-1}}$, was subtracted from all velocity measurements obtained for the cube.

The derived stellar velocities were assessed based on a reliability flag following the method described in section 3.2 of Giesers et al. (2019). This includes considering the signal-to-noise ratios of the extracted spectra or the agreement between the velocities derived from cross–correlation and spectral fit. Only velocities with a reliability grading above 80 per cent were kept. Further, we considered the agreement between the magnitudes recovered from the spectra and those provided in the HST catalogues, as large discrepancies could indicate contamination in the spectra by nearby stars. PAMPELMUSE expresses the photometric agreement as a *MagAccuracy* parameter, ranging from 0.0 (large discrepancy) to 1.0 (perfect agreement). We imposed a cut value of 0.6.

The final step in the data analysis was a calibration of the uncertainties of the LOS velocity measurements. To do so, we followed the approach outlined in Kamann et al. (2018), which makes use of the different valid velocity measurements available for each star and is based on the expectation that in the absence of intrinsic variability, the normalized scatter of these measurements should follow a Gaussian distribution with a standard deviation of unity. Following this calibration, we averaged the filtered velocities per star, using inverse-variance weighting.

After extracting the reliable velocities, 38 602 stars were left in our sample, including the NFM and WFM data. To compare the depth of the NFM data, we plot stars within 20 arcsec, which include 963 NFM stars and 1552 WFM stars, on the CMD of Fig. 2. We used the ACS photometry for the CMD, which has photometry in the F606W and the F814W filters. The completeness histograms show the comparison of number counts in the WFM and NFM samples relative to the HST catalogue within the NFM region. We found that the NFM data is complete for stars brighter than 19.5 mag, which excludes ∼10 stars that are on the edges of the pointings in these comparisons. For the WFM data, we are complete below 18 mag. 50 per cent of the stars are below 18.6 mag in WFM mode whereas, in the NFM data, 50 per cent of the stars are below 19.8 mag, which is close to the completeness limits. The mass range covered by the NFM data is also broader since more stars with lower masses (down to 0.5 $M_\odot$) are included. The masses of the stars were obtained based on the isochrone comparisons as mentioned above. There are no observations for the WFM data below 20 mag, whereas the NFM data extends down to the 22nd magnitude. But, further away from the centre, the WFM data reach a similar depth due to longer exposure times and lesser crowding. The data set covers everything from the tip of the RGB to 4 mag below the main-sequence turn-off. The median S/N is ∼12 for the NFM data and the median velocity uncertainties are ∼2.3 km s^{-1}. For stars around 16 mag, the typical uncertainties in velocities are ∼1 km s^{-1}, whereas, for a star of magnitude ∼21 mag, the uncertainties increase to ∼5 km s^{-1} because of the low S/N. The 50 per cent completeness limit in the F606W magnitude and the masses are 18.6 mag and 0.71 $M_\odot$, respectively, for the WFM data. For NFM data, the 50 per cent completeness limit is 19.8 mag and 0.65 $M_\odot$.

The membership probability of the stars being a part of the cluster was estimated using the procedure described in Kamann et al. (2018). Briefly, we assume that the observed stars are composed of cluster members and a field population. For the former, we assume that its velocity and metallicity distributions can be approximated as Gaussians, whereas for the latter, we use the Milky Way model by Robin et al. (2003) to predict velocities and metallicities. We then iteratively determine the likelihood of each star belonging to the cluster or field population, with the additional constraint that the fraction of cluster stars decreases monotonically with distance to the cluster centre. The membership probability is then assigned to each star and those with a probability lower than 0.6 are excluded from our analyses. Although ω Centauri has a metallicity spread of more than a factor of 10 (e.g. Johnson & Pilachowski 2010), it has a radial velocity that offsets the member stars from those of the MW stars. For a more detailed description of the method, see Walker et al. (2009) and Kamann et al. (2016). We also excluded the stars with temporal variations in their LOS velocities that can be potential binary stars. We use the probabilities that were derived by using the method described in Giesers et al. (2019). This work will be presented in Wragg et al. (in preparation).

The final sample of stars that were used in the analysis of the central kinematics excludes non-member stars with a cluster membership probability cut of <0.6, a binary variability probability >0.7, and an S/N cut of <8 for the mean of the extracted spectra, which leaves us with 28 108 stars of which 936 are NFM stars.

3 KINEMATIC DATA

We analyse the LOS velocities in this section within the half-light radius of ω Centauri and create velocity and velocity dispersion radial profiles. This will help further study of a possible IMBH in ω Centauri. The centre of ω Centauri is debated in the literature and several centres have been proposed based on photometry and kinematics.

3.1 Existing analyses and proposed centres

A putative BH in ω Centauri was reported in NGB08, and the centre was estimated using the surface density counts of stars in the central 40 arcsec of HST/ACS data. The kinematic data was obtained from GMOS integral-field spectroscopy with a spectral resolution of $R = 5560$ Å; in the Ca-Triplet region (7900–9300 Å), and the LOS velocities were derived using these spectra. Their data set was seeing-limited, whereas the NFM data is at a resolution of 25 mas. The field-of-view (FOV) is also bigger covering the half-light radius of the cluster. Based on the line-of-sight velocity dispersion (LOSVD) measurements from GMOS IFU and a clear cusp in the surface brightness profile, an IMBH of $M_{BH} = 4.0^{+0.75}_{-1.0} \times 10^4$ $M_\odot$, and a LOS central velocity dispersion, $\sigma_{LOS} = 23.0 \pm 2.0$ km s^{-1} were reported for this cluster. The measured cusp in the surface brightness profile was in agreement with the theoretical predictions from *N*–body simulations in Baumgardt, Makino & Hut (2005) for clusters harbouring IMBHs, where the central BH tends to prevent the core collapse.

vdMA10 presented another analysis for the central few arcmins, where they estimated the projected number density distribution of ∼10^6 stars from HST photometry. The LOS velocities were obtained using the ground-based data from Suntzeff & Kraft (1996); Mayor et al. (1997); Reijns et al. (2006). Proper motions were also estimated using ground-based data from van Leeuwen et al. (2000) and also using 10^5 stars from HST data (Anderson & van der Marel 2010). The centre of the cluster was determined using three independent ways and found to be offset from the one derived in NGB08 by 12 arcsec. Their analysis did not confirm the density cusp that was observed in NGB08 due to the offset centre. Anisotropic models were fit to the data wherein if a flat core was assumed, a no-BH model provided a good fit, whereas cuspy models required either an IMBH of $M_{BH} = 8.7 \pm 2.9 \times 10^3$ $M_\odot$ or a dark cluster of size $\lesssim 0.16$ pc. The final result was an upper limit on a possible IMBH with $M_{BH} \lesssim 1.2 \times 10^4$ $M_\odot$ at 1σ confidence level, in strong tension with the IMBH mass suggested by NGB08.

A third search for a central IMBH was performed in N10 where they obtained additional integrated field spectroscopy for the central region of the cluster using VLT-FLAMES/ARGUS. These observations have a spectral resolving power of R∼10000 and cover the 820–940 nm region using the GIRAFFE spectrograph with a FOV of 11.5 arcsec × 7.3 arcsec. They combined the new LOS velocities derived from the Ca-Triplet region with the existing measurements from NGB08 and estimated a different centre from the additional kinematics. A peak in the velocity dispersion map was found by running a 5 arcsec kernel across the 2-D map of velocity dispersion, which was their estimated centre for the cluster along with a measured central velocity dispersion of 22.8 ± 1.2 km s^{-1}. Using isotropic

Table 2. Existing and current measurements of ω Centauri.

	Centre RA	Centre Dec	M_{BH} ($M_\odot$)	σ_{LOS} (km s^{-1})
NGB08	13:26:46.04	−47:28:44.8	$4.0^{+0.75}_{-1.0} \times 10^4$	23.0 ± 2.0
vdMA10	13:26:47.24	−47:28:46.5	$\lesssim 1.2 \times 10^4$	–
N10	13:26:47.11	−47:28:42.1	$4.7 \pm 1.0 \times 10^4$	22.8 ± 1.2
Kinematic centre (From rotation)	13:26:47.31	−47:28:51.4	–	19.3 ± 1.4
Dispersion centre (From dispersion)	13:26:46.86	−47:28:42.5	–	22.6 ± 1.5

Note. The first three rows list the existing measurements of ω Centauri made in NGB08 (Noyola, Gebhardt & Bergmann 2008), vdMA10 (van der Marel & Anderson 2010), and N10 (Noyola et al. 2010). The bottom rows present measurements derived in this work, which are described in Section 5.1.

dynamical models and their kinematic centre, they estimated a central BH of $M_{BH} = 4.7 \pm 1.0 \times 10^4$ $M_\odot$.

The above-mentioned measurements using various centres are listed in Table 2. The NGB08 centre is offset by 12 arcsec from the vdMA10 centre. The N10 and vdMA10 seem to lie approximately on the rotation axis of the cluster but are ∼3 arcsec apart (see Fig. 3). Further analyses using these centres are presented in the subsequent sections.

3.2 Analysing the MUSE kinematics

To study the dynamics of ω Centauri, we created radial profiles of the velocity dispersion and the rotation velocity using two methods. In the first method, we radially binned the stars, where each bin consisted of a minimum of 100 stars, and covered a radial range of $\log(r/1 \text{ arcsec}) > 0.15$. In the second method, we created analytical profiles for the cluster to estimate the rotation and LOSVD. For both methods, a maximum likelihood approach (Pryor & Meylan 1993) was used in combination with the Markov chain Monte Carlo (MCMC) algorithm EMCEE (Foreman-Mackey et al. 2013) to estimate the quantities. A detailed description of this analysis is given in Kamann et al. (2018). For the maximum likelihood analysis, we assumed the probability of finding a star with a velocity $(v_i \pm \epsilon_i)$ at a projected distance r_i from the cluster centre to be:

$$p(v_i, \epsilon_i, r_i) = \frac{1}{2\pi\sqrt{\sigma_r^2 + \epsilon_i^2}} \exp \frac{(v_i - v_0)^2}{-2(\sigma_r^2 + \epsilon_i^2)}. \quad (1)$$

Here, $\sigma_r = \sigma_r(r_i)$ and $v_0 = v_0(r_i)$ are the dispersion and heliocentric radial velocity of the cluster, respectively, at the position of star i. We then found the values of σ_r and v_0 that minimized the negative log-likelihood of the model given the kinematic data. A limitation of this approach is that it applies to the stellar systems whose LOSVD is Gaussian ignoring the higher moments of the LOSVD. For determining the rotation velocity of the cluster, we assume that the cluster is a rotating disc and add an angular dependence (θ) to the mean velocity in equation (1):

$$v_0 \rightarrow \overline{v}(r_i, \theta_i) = v_0 + v_{rot}(r_i)\sin(\theta_i - \theta_0(r_i)), \quad (2)$$

where v_{rot} and θ_0 are the projected rotation velocity and axis angle. This allows us to estimate the LOS velocity in each bin radially from the cluster centre. We then implemented the MCMC analysis to minimize the negative likelihood in every radial bin and ran a total of 100 chains with 100 steps for each bin, which is sufficient for determining the parameters. We constrained three parameters, σ_r, v_{rot}, and θ_0 with uniform, uninformative priors.

Since the effect of binning is removed while using the analytical forms, we create the analytical profiles using the following functional form for the rotational velocity, v_{rot}:

$$v_{rot}(r) = \frac{2v_{max}r}{r_{max}} \Big/ [1 + (r/r_{max})^2]. \quad (3)$$

The v_{rot} profile is based on the prediction for a system undergoing violent relaxation (Lynden-Bell 1967) and has been previously used to model the rotation profiles of star clusters in, e.g. Bianchini et al. (2018).

Here, three parameters were constrained: the peak amplitude of the rotational velocity, v_{max}; the radius at which v_{max} occurs, r_{max}; and θ_0. Using the MCMC analysis as mentioned above, we fitted those parameters for a total of 100 chains and 500 steps and created radial profiles based on the median values and the 16th and 84th percentile of the distributions. The results of these methods applied to the data are discussed and presented in Section 5.2 and Fig. 5.

4 A COUNTER-ROTATING CORE IN ω CENTAURI

In this section, we analyse the central 100 arcsec in detail with a focus on the central 20 arcsec as this area is covered by the NFM data.

4.1 Creating kinematic maps

To study the mean LOS velocity as a function of position, we used a supervised neighbour-based learning method to create a smoothed velocity map. We used a *K*-nearest neighbours (KNN) analysis, where the basic principle is to group the stars based on a metric (Pedregosa et al. 2011). Here, the grouping classifies the nearby neighbours based on their distances and we estimated those using `biweight_location` (Beers, Flynn & Gebhardt 1990) of ASTROPY, which performs a robust detection of the mean of the distribution, in this case, the LOS velocities of the stars.

In this method, the number of samples (k) is defined as the number of neighbours that would be chosen to represent a group. A smaller k-value selects fewer neighbours and results in a coarser grouping whereas a higher k-value provides smoother grouping. At first, standard Euclidean distances are calculated between the neighbours based on the k-value, and then a maximum radius is given within which the grouping needs to be performed. We visually inspected maps of the KNN-based mean velocities with k-values ranging from 40–300. We found that smaller values of k (<200) lead to patchiness of the velocity maps due to the lesser number of stars in each group (e.g. see Fig. A1). Therefore, we used a k-value of 300 to derive the LOS velocity map, where the large-scale rotation of ω Centauri is visible (see Fig. 3, left column). A zoomed-in version shows the central 20 arcsec of the core (Fig. 3, left middle panel), mainly

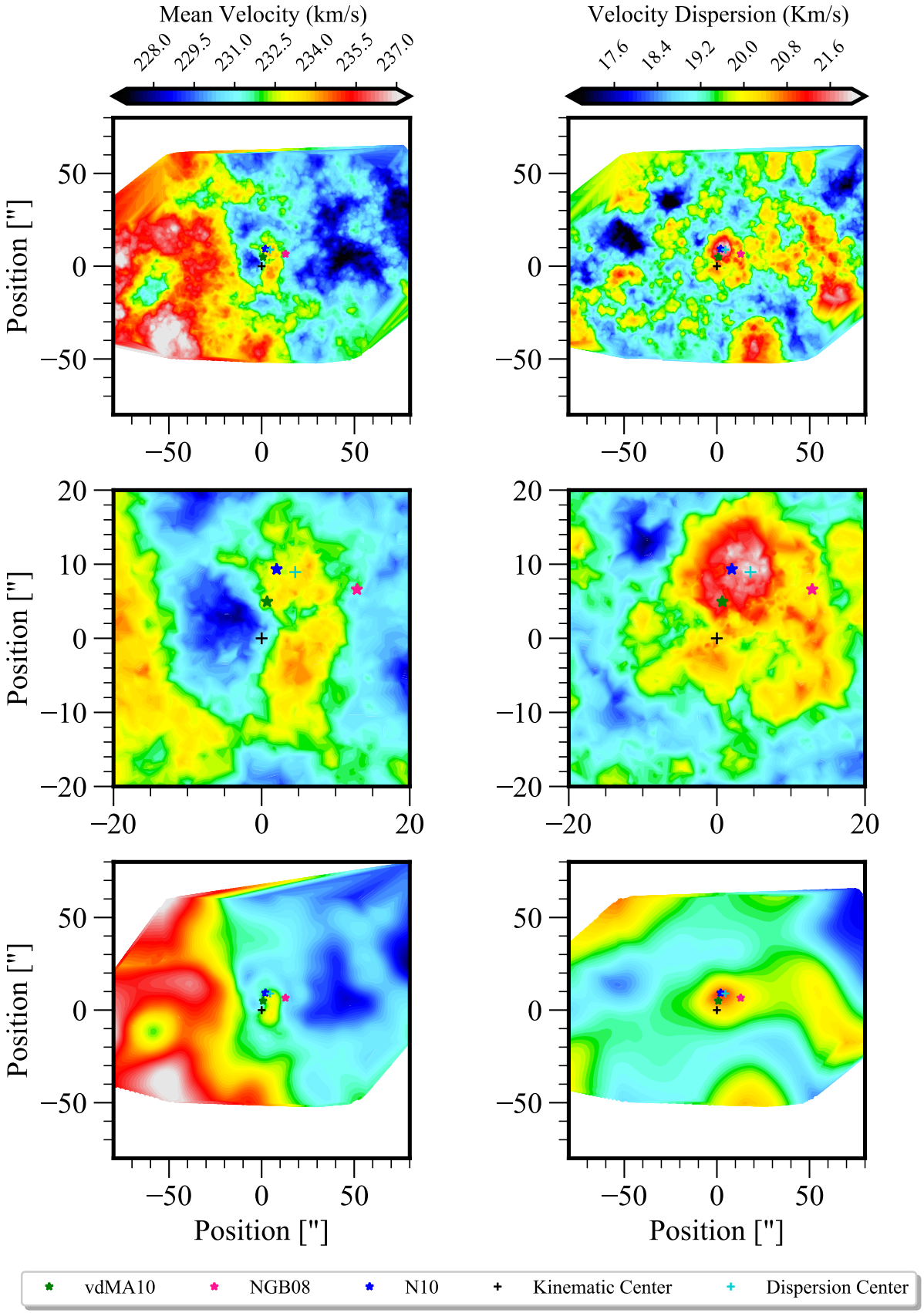

Figure 3. Rotation and velocity dispersion maps: Top and middle panels: Rotation velocity and velocity dispersion maps of the central 80 arcsec and a zoomed version of the central 20 arcsec of the MUSE WFM and NFM kinematics grouped using KNN with a *k*-value of 300. Bottom panel: LOESS smoothed 2D maps of the rotation and dispersion. Different centres are marked in different colours as indicated in the legend.

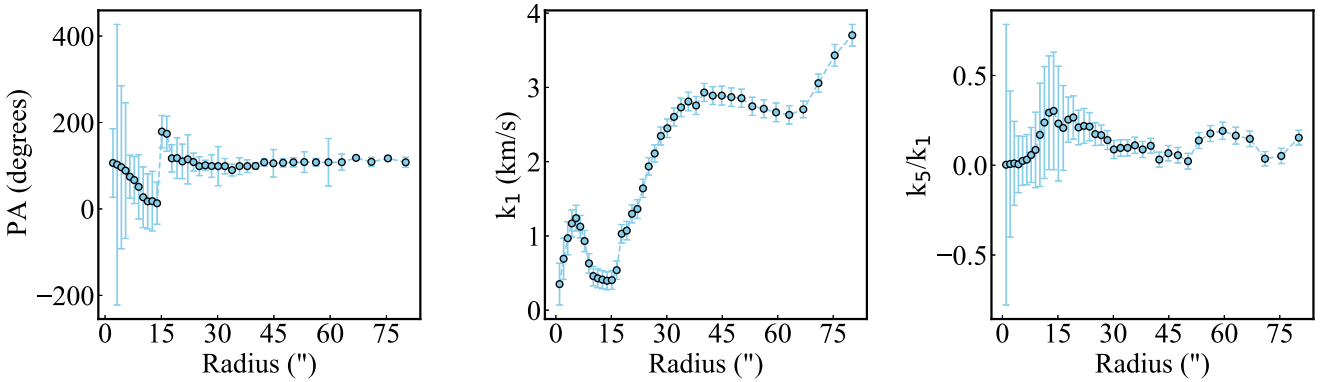

Figure 4. Kinemetry results for the central 80 arcsec of the cluster using the LOESS maps. Left: The PA of the cluster, measuring the change in the velocity structure on the map. Middle and right: The coefficients k_1 and k_5/k_1 from the Fourier expansion of the velocity field for the best-fitting ellipse. k_1 describes the bulk motion of the cluster with a peak at ∼5 arcsec and decreases after that. Then it increases with the radius indicating the global rotation of the cluster. k_5/k_1 is peaked at ∼15–20 arcsec, which indicates the rotation components within the map.

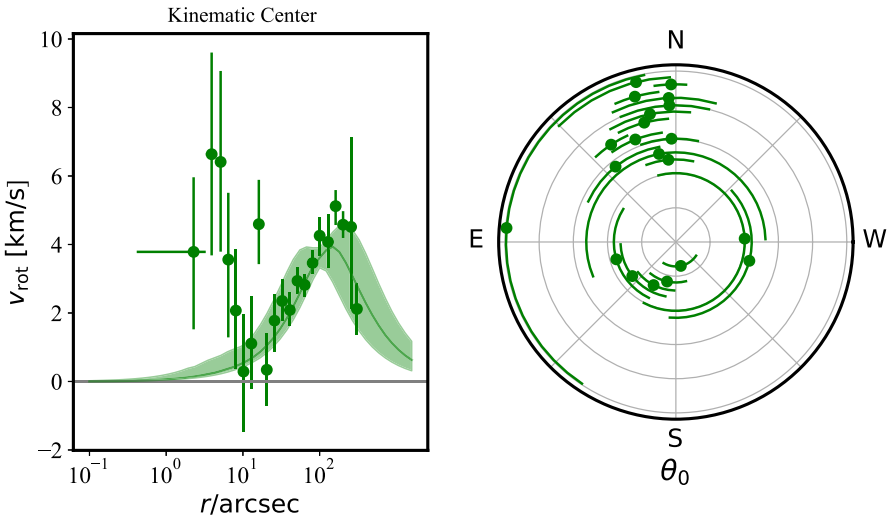

Figure 5. Left: Rotation profile of the cluster using the kinematic centre. Solid points are the result of discrete binning of the radial velocities (equation 3) whereas the shaded curve is the analytical rotation profile. Right: PA of the rotation of the cluster. Note the counter-rotation observed towards the centre.

covered by the NFM data, which is counter-rotating with respect to the global rotation of the cluster. The central 100 arcsec of ω Centauri are rotating with maximum projected velocities of ∼4 km s^{-1} and the inner core within 20 arcsec shows maximum rotational velocities of ∼3–5 km s^{-1}. The different centres from the literature are marked here, with each centre being a few arcsec apart. Other estimates of the centres based on our velocity and dispersion maps are also marked, which we discuss in the next subsection.

For a better visualization of the velocity maps with less noise, we employed another method to derive the velocity map of the cluster; the locally weighted regression (LOESS) technique, which was introduced in Cappellari et al. (2013) based on an algorithm developed by Cleveland (1979) for the 1D case and further improved for the 2D case in Cleveland & Devlin (1988). This is a regression method that uses a multivariate smoothing analysis on a surface by the local fitting of the function in a moving way similar to the moving average. This method robustly determines the mean values of the underlying parameters in case of noisy data. In our case, the parameters are the LOS velocities and the noise is the velocity dispersion of the stars. We used the code `loess_2d` from Cappellari et al. (2013), which requires input velocities, and a regularization factor (f) that describes the fraction of points that are considered for the approximation and controls the amount of smoothing of the map. We used a value of $f = 0.1$ and assumed a linear approximation to determine the LOESS smoothed maps. The bottom panel of Fig. 3 shows the LOESS map of the LOS velocities within 80 arcsec around the cluster centre. The result is consistent with the maps from the KNN analysis. On a larger scale, the global rotation is dominant and as we go towards the centre, the counter-rotation is visible. The different centres are marked similarly as in the KNN maps, and we observe that except for the NGB08 centre, the rest of the centres are aligned close to the rotation axis of the counter-rotating core. It is worth noting that the NGB08 centre is also close to the zero velocity curve (green contour) of the counter-rotation, but on the other side, which is a local minimum.

In both maps, there is clear evidence that the rotation in the central region of the cluster is misaligned with the rotation at large radii. This counter-rotation dominates the kinematics within the central 10–20 arcsec and appears to be centred south of the vdMA10 and N10 centres. To check for the effect of contamination from any bright stars, we removed stars brighter than 14th magnitude in the F625W filter. We found that there are two bright stars

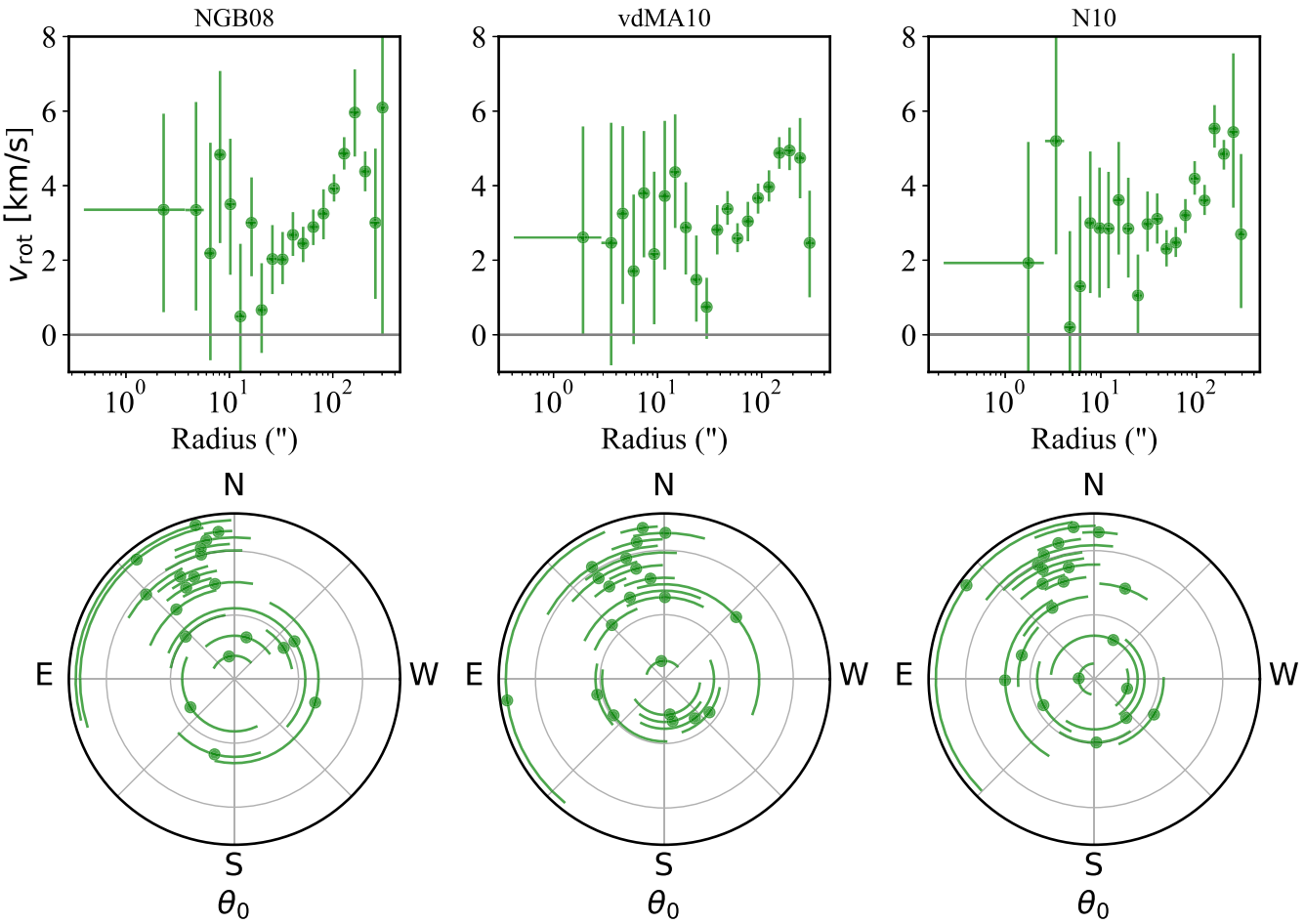

Figure 6. Rotation profile and PA of the rotation of ω-Cen. The top panels show the rotation (amplitude) profile of the stars that are binned radially using the method in Section 3.2. The bottom panels show the orientation of the rotation axis within each radial bin. From left to right: profiles using N10, vdMA10, and NGB08 centres. Note that the counter-rotation is only observed in vdMA10.

at the centres of the counter-rotating velocity components both moving in the same direction with a velocity of ∼20 km s^{-1} but the counter-rotation signal is still significant even after removing the stars.

Apart from the LOS velocities, we also analysed the velocity dispersion of ω Centauri using KNN analysis. Here we grouped the stars and used the statistic `biweight_scale` from ASTROPY, which determines a robust standard deviation of the distribution of stars, i.e. a velocity dispersion in this case. We also used different k-values ranging from 40 to 300. A lot of peaks or patchiness was detected across the entire velocity dispersion map for smaller k-values (see Fig. A1). But, as we grouped more stars, for a k-value of 300, we found a prominent central peak. This is shown in the right column of Fig. 3. This peak is close to the centre from N10 as expected since their centre was derived based on the peak in the velocity dispersion. The remaining centres are also marked similarly to the ones in the velocity maps. The bottom-most panel shows the LOESS smoothed map that was derived based on the KNN velocity dispersion map, where the central peak is visible. When we compare the mean velocity and the velocity dispersion maps in the middle panel, the peak in the central velocity dispersion appears to be offset from the rotation axis of the counter-rotating core. We quantify this rotation and dispersion in the subsequent sections and constrain different centres based on them.

4.2 Quantifying the counter-rotation with kinemetry

To quantify the velocities and rotation, we performed *kinemetry* on the velocity and dispersion maps of the cluster. We used LOESS maps for this analysis only as an alternative to the KNN maps to test if the counter-rotating core is real and quantifiable using kinemetry. *Kinemetry* is a method from Krajnović et al. (2006) that performs a harmonic expansion of 2D kinematic moments, in our case, mean local velocities that are the first kinematic moments, along a set of best-fitting ellipses on the map.

When analysing velocity maps, kinemetry assumes that there are ellipses along which the velocities can be described with a simple cosine law,

$$V(R, \psi) = V_0 + V_c(R)\sin(i)\cos(\psi), \quad (4)$$

where V_0 and V_c are the systemic and circular velocities, projected on the sky at an inclination i, and traced along the ellipse via the azimuthal angle ψ, measured from the projected major axis. Equation (4) is strictly correct for disks in which stars move on circular orbits, but Krajnović et al. (2008, 2011) showed that it applies to a large fraction of early-type galaxies, with deviations of less than 5 per cent. The kinemetric analysis of the velocities along an ellipse is performed

by evaluating the harmonic terms:

$$K(a,\psi) = A_0(a) + \sum_{n=1}^{N} A_n(a)\sin(n\psi) + B_n(a)\cos(n\psi), \quad (5)$$

where a and ψ are the semi-major axis and the azimuthal angle, and in the case of the velocity, n is an odd number. The best-fitting ellipse is determined by minimizing the A1, A3, and B3 terms, as they define the shape and the orientation of the ellipse. Kinemetry results are often presented in a compact form:

$$K(a,\psi) = A_0(a) + \sum_{n=1}^{N} k_n(a)\cos([n(\psi - \phi_n(a))], \quad (6)$$

where $k_n = \sqrt{A_n^2 + B_n^2}$ and $\phi_n = \arctan(A_n/B_n)$. In this form the term k_1 describes the amplitude of the rotation, while k_5 is the first non-minimized higher order coefficient which defines the deviations from a simple rotation as assumed in equation (4). For further details regarding *kinemetry*, we refer to Krajnović et al. (2006).

For the kinemetric modelling, for the initial models, we fixed the centre of the cluster to an initial guess from the previous section. Since the photometric axis ratio of ω Centauri is above 0.8 at all radii (Geyer, Hopp & Nelles 1983), we limited the shape (axial ratio) of the ellipses for the kinemetry to be between 0.7 and 1.0. To increase the range of the fit, we used a cover value of 0.6, which means that 60 per cent of the points on the ellipse should be present for the ellipse to be included in the fit. We also fixed the range for the PA from 0° to 180°. The results from these fits are shown in Fig. 4.

The left panel of Fig. 4 shows the PA that is varying with respect to the radius and twists at ∼15–20 arcsec by 180° approximately indicating the observed counter-rotation. The errors on the PA of the data points below 5 arcsec are large and can be ignored because the counter-rotation is on a scale of 15 arcsec and the ellipses fitted on a scale smaller than 5 arcsec are unable to trace the rotation. The k_1 coefficient tracing the rotation shows a small peak at 5 arcsec delineating the extent of the counter-rotation followed by the global rotation of the cluster. The large error bars on k_5, due partially to the very low-level rotation of the cluster, make it almost consistent with 0 and prohibit further analysis of the deviations. The peak in k_5 at ∼20 arcsec is correlated with the drop in k_1, as is expected at the edge of a kinematic component (Krajnović et al. 2006). Together with the radial variation of the PA of ellipses (Fig. 4, left), which stabilizes at the end of the counter-rotating core, $k_1 \sim 0$, and where the error in k_5 significantly drops, kinemetry analysis quantifies the extent and the shape of the central counter-rotation in ω Centauri. To constrain the centre, we explore the central 20 arcsec with different techniques in the next section.

5 KINEMATIC CENTRE AND COMPARISONS WITH THE PREVIOUS STUDIES

In this section, we describe various methods that were used to determine the centre for this cluster and then use it to compare it with the previously published centres.

5.1 Finding the kinematic centre

A well-defined centre is crucial in determining the velocity dispersion and rotation profiles, which are required for the detection of any kind of dark mass in the cluster centre. Below, we show that using several methods, we are unable to numerically constrain the centre to better than ∼5 arcsec, within the range of previous estimates. The kinematics near the centre are so complex that the result also depends on the method we use. However, assuming that the counter-rotation represents the centre, we constrain the centre to be at RA= 13h 26m 47.31s and Decl $= -47°28'51.39''$ with an uncertainty of ∼5 arcsec along the declination. This position is closest to vdMA10, while the centres N10 and NGB08 centres are not consistent with being at the centre of the counter-rotating core. We describe each of the methods attempted to better constrain the centre below; all of these are consistent with our centre quoted above, with uncertainties ranging from 5 arcsec to 20 arcsec.

The first method we implemented was a slight modification to the MCMC analytical profile fits described in Section 3.2. Here, we added two additional parameters to the MCMC analyses, dx and dy as offsets to the centre and fit them in the iterations. We provided an initial guess for the centre by eye based on the counter-rotation from the velocity map of the KNN analysis and allowed it to vary as offsets in dx and dy. We fit the centre for every radial bin and based on several runs, we found that the best-fit median of the centre was not very well constrained. Although dx and dy are scattered around zero, the average errors ranged up to 20 arcsec, which is our entire region of counter-rotation. To test the accuracy of this method, we used a sample test case of M80 using the data published by Göttgens et al. (2021), where the centre was constrained using a similar MCMC analysis of their Jeans' models. The dx and dy offsets that we obtained were similar to those found in Göttgens et al. (2021), with median errors up to 2 arcsec. We conclude that this method is most likely not suitable for ω Centauri, due to the flatness of the core and the counter-rotation present close to the centre.

We tried an approach using the pie-slice method, a similar approach that was used in Anderson & van der Marel (2010), where they used the number counts of the stars to determine the centre whereas we use the LOS velocities instead of the photometry. This method determines the point around which the stellar kinematics are most symmetrically distributed. First, we provide the same initial guess that was used in the previous method as a trial centre. Based on this centre, a 5 arcsec grid of trial centres is created around it. Around each grid point, we constructed 16 azimuthal wedges, extending to distances of 20 arcsec, and each wedge was further divided into 7 radial bins. We minimized the differences between the mean velocities in opposite pairs of bins along with the uncertainties using the `biweight_location` robust statistic (described in Section 4.1). Finally, we summed up these differences for all the bins to determine a χ^2 measure. This method yielded a χ^2 minima along the rotation axis of the counter-rotation of the cluster and hence appears not suited for locating the centre of ω Centauri.

Finally, we used an approach based on kinemetry, where we performed a grid search using the centre as two variables. We divided the central 20 arcsec into a grid of 30 centres and performed kinemetry using each centre. Each centre was fixed in the code along with the PA and the flattening (q) of the ellipses. To obtain the initial values for PA and q, we first ran the kinemetry code with our initial guess for the centre and averaged the PA and q of the ellipse at ∼3 and ∼5 arcsec. We used this value PA $= 80°$ and $q = 0.84$ for fixing the PA and q of the ellipses. To avoid the effects of the global rotation, we limited the number of ellipses to 9. and then performed kinemetry on the grid of centres. We estimated the χ^2 for the last three ellipses by minimizing the sum of the squares of their coefficients A1, A2, B2, A3, and B3 (Jedrzejewski 1987; Krajnović et al. 2006). We found that two local minima existed for the χ^2 along the counter-rotating axis that lies ∼1.5 and ∼7 arcsec from our initial guess. We used a mean of both the centres to get an estimate for the final centre with a final uncertainty estimate of ∼5 arcsec in the declination and ∼1.5

arcsec in the right ascension. The uncertainty was estimated using the 1σ map of the χ^2 for a $\Delta\chi^2 = 2.3$. Hereafter, we refer to this centre as the kinematic centre.

Based on this result and our earlier approaches to determining the centre, we found that the location of the centre is always degenerate along the rotation axis. The vdMA10 centre that lies along this rotation axis has the potential to be one of the possible centres as it is the closest to our derived centre and is within the median uncertainties of 5 arcsec.

We also estimated a centre based on the LOESS dispersion maps from Fig. 3. For using kinemetry on the dispersion maps, the profile is assumed to be constant and the corresponding coefficients are minimized. In this case, the dispersion maps are assumed to be point symmetric (refer Krajnović et al. (2006)), and since we are not analysing the rotation, we used circles instead of ellipses with a PA of 0°. We then minimized the sum of the square of the coefficients A1, A2, B1, B2, A3 and B3 to obtain the χ^2. Here, A_0 provides an estimate of the velocity dispersion, which is 22.6 ± 1.5 km s^{-1}. We similarly performed kinemetry as previously mentioned and used the χ^2 estimate to determine the centre. We estimated the centre to be RA = 13h 26m 46.86s and Decl = -47° 28′ 42.46s with an uncertainty of 1.5 arcsec. Hereafter, we refer to this centre as the dispersion centre. The uncertainty is estimated similarly as determined previously using the χ^2 map. This dispersion map based centre is closest to the N10 centre and is ∼2.5 arcsec away from it. Although, there is a significant offset (∼10 arcsec) between the counter-rotation centre and the dispersion centre, both the centres are closest to the vdMA10 and N10 centres, respectively. On the contrary, the offset in the NGB08 is the largest. All the centres and corresponding central dispersion values are listed in Table 2.

5.2 Kinematic profiles for the various centres

We choose our derived centre from the counter-rotation i.e. kinematic centre for the rest of the analysis. We do not use the centre from dispersion in our analyses as it is close to the N10 centre and results in similar profiles. We used the kinematic centre to derive the rotational velocity profile, dispersion profile, and the PA of the rotation as shown in Figs 5 and 7. These profiles were derived using the method described in Section 3.2. The solid points in Fig. 5 are a result of the discrete binning of the radial velocities whereas the curve is the analytical profile of the rotation (from equation 3). In the rotation plot of the cluster, we see the signal for a counter-rotating core, where the PA of the velocities close to the centre (within 20 arcsec) is in the opposite direction to the global rotation of the cluster. The PA for the inner 15 arcsec has a mean of 136° E of N with a scatter of 20° whereas the PA > 20 arcsec is ∼10°. The maximum rotational velocity of the inner 15 arcsec is 3–5 km s^{-1} whereas the outer rotational velocity peaks at ∼4.5 km s^{-1}.

We also created radial profiles of the rotational velocity and velocity dispersions for the existing centres proposed in NGB08, vdMA10, and N10 using the same method. They are shown in Figs 6 and 7. We observe that there is no significant counter-rotation around the NGB08 centre. This is because the centre is ∼12 arcsec away from the other centres and further away from the counter-rotating core (see Fig. 3). This is also visible in the PA plot where the innermost data points (within 10 arcsec) are scattered around in all directions, whereas the rest show a global rotation for the cluster ∼19° E of N. The rotation curve around the vdMA10 centre again shows a scatter close to the centre without any distinctive peak but the PA plot shows a clear counter-rotating signal, which is similar to what we find for the kinematic centre. The velocities within 10 arcsec have a mean PA of 208° ± 21° E of N except for the central data point and the rest of the velocities have a PA similar to the one from the previous centre with a mean of 10° ± 15°. The velocities within 10 arcsec from the N10 centre are similar to those from the vdMA10 centre but the PAs are scattered around in all directions, with some of the data points in the opposite direction compared to the global rotation. They have a mean of ∼200° but have a standard deviation of ∼60° which is much larger compared to the vdMA10 centre. The rotation profiles at larger radii (>20 arcsec) for all the centres behave similarly as expected in GCs (e.g. Fiestas, Spurzem & Kim 2006), including a detailed study of ω Centauri in van de Ven et al. (2006). According to equation (3), we expect a maximum at a few half-light radii and then a steady decrease for larger radii. This trend was observed for 25 GCs in Kamann et al. (2018), where detailed rotation and dispersion profiles were derived. We observe a similar trend, but in addition, there's also an increase in the rotational velocity close to the centre in our estimates of ω Centauri due to the presence of counter-rotation in Fig. 5.

Fig. 7 shows the comparison between the observed dispersion profiles derived for different centres. First, we compared the dispersion profiles from the previously published data in NGB08, vdMA10, and N10 with the dispersion profiles derived using the MUSE data for the same centres as used in those studies. The data from NGB08 consisted of only two data points from their observations using the GMOS-IFU. The measurements in N10 were done using the ARGUS IFU with FLAMES on VLT whereas the measurements for vdMA10 were taken from the HST proper motions that were estimated by Anderson & van der Marel (2010). We used a distance of 5.2 kpc (Harris 1996) for ω Centauri to scale the proper motions to the LOS velocity dispersions. We found surprisingly similar trends with respect to each study within the error bars. The N10 result has a rise in the central velocity dispersion that we observe from our data too; this favours the presence of a $\sim 10^4$ $M_\odot$ BH from the N10 analysis. The dispersion profiles from NGB08 and vdMA10 show a ∼11 and ∼22 per cent drop for the centre-most data point, respectively, compared to the N10 observations, but follow a similar trend in both profiles. Other than the N10 profile, all profiles seem consistent with a constant dispersion of ∼20 km s^{-1} in the central 10 arcsec, since from the velocity dispersion map, the centres are offset from the peak and lie close to the counter-rotation axis. The rightmost bottom panel of Fig. 7 includes the dispersion profile using our kinematic centre along with the other dispersion profiles based on the MUSE data only. Including the uncertainties in the other profiles, the velocity dispersion rises smoothly towards the centre up to a central velocity dispersion of ∼20 km s^{-1}, which is similar to other studies. There is no specific rise as observed in N10 though, which is mostly dependent on the assumed centre.

To quantify this rise in dispersion, we did a linear regression on the data within 15 arcsec for the dispersion values using the code from Kelly (2007), which takes into account the measurement errors in the y-direction and estimates the scatter in the regression. We found variable slopes for each centre with the highest slope of -3.9 ± 1.8 km s^{-1} arcsec for the N10 centre. The slope for the vdMA10 centre was found to be -3.2 ± 1.9 km s^{-1} arcsec. This is almost similar to the N10 centre because the majority of the points rise but the central data point drops to 18 km s^{-1}. On the contrary, we found a zero to positive slope for the NGB08 centre with a value of -0.3 ± 3.1 km s^{-1} arcsec. The slope for our kinematic centre was -0.3 ± 4.2 km s^{-1} arcsec. From our regression analysis, we have a significant scatter for the slopes for each centre especially for the NGB08 centre and the kinematic centre. Although they all

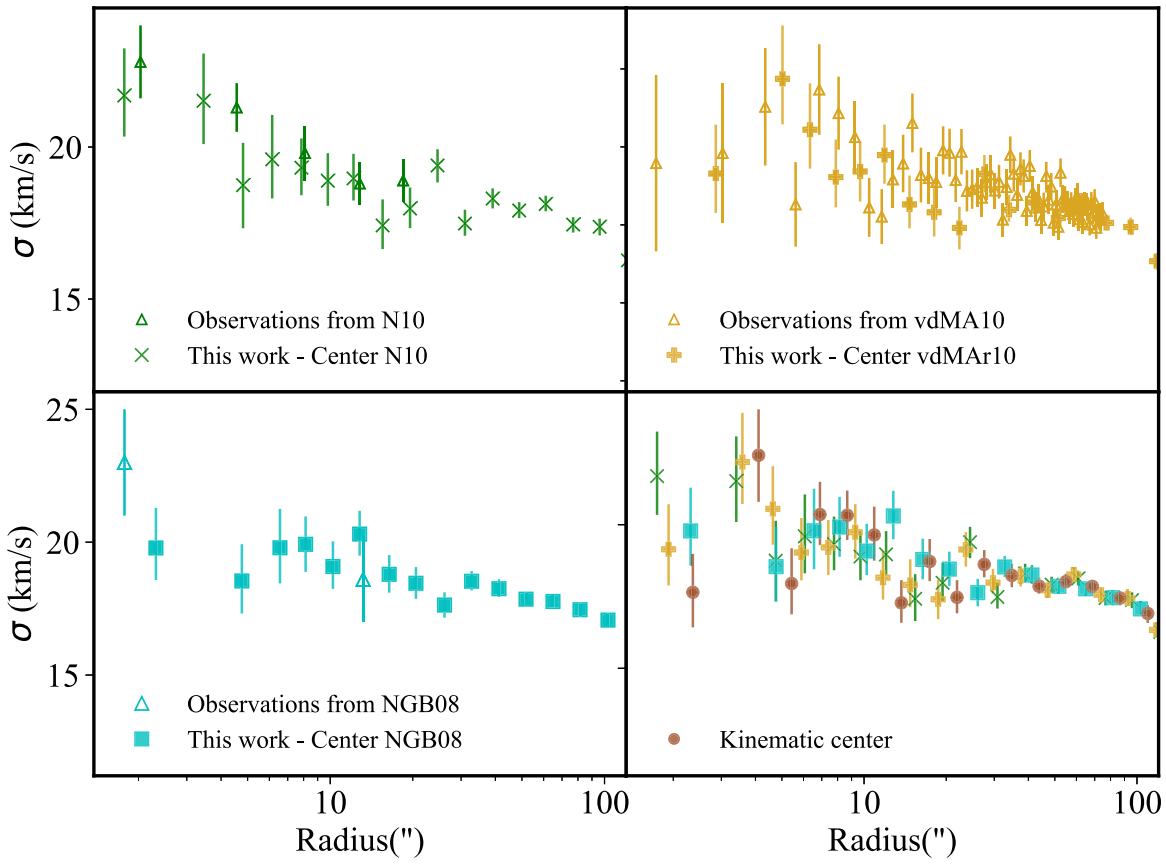

Figure 7. Comparison of the velocity dispersion profiles. Open triangles in green, orange, and blue are observations from the NGB08, vdMA10, and N10. Other symbols in green, orange, and blue are the radially–binned velocities from this work for different centres. Note that our measurements match the overall dispersion profiles well from each study. The bottom right panel shows the velocity dispersion profile (brown solid circles) derived using the kinematic centre (centre from the counter-rotation) in this work. The other three profiles are the same as shown in the rest of the panels and are plotted for comparison with the kinematic centre's profile.

were found to lie within 1σ significance of each other, there are differences in the velocity dispersions within the central 5 arcsec from each centre. For the N10 centre and the vdMA10 centre, we estimated the integrated central velocity dispersions (<5 arcsec), which were 20.6 ± 0.9 and 20.9 ± 0.7 km s^{-1}, respectively. For the NGB08 centre, it was 18.9 ± 1.0 km s^{-1}, whereas for the kinematic centre, it was 19.6 ± 0.9 km s^{-1}. The highest difference was found to be between the NGB08 centre and the vdMA10 and N10 centres. The differences in these central velocity dispersions can indeed make a difference in the detection of an IMBH from the previous studies. A detailed dynamical modelling using the different centres and the dispersion profiles is needed to quantify the presence/absence of an IMBH.

Another aspect that can be observed from the comparison of the dispersion profiles is that LOS velocity measurements from different types of observations such as integrated-light measurements or resolved stellar velocities result in similar velocity dispersion measurements. In the literature, such as Lützgendorf et al. (2015), significant changes between velocity dispersion measurements were found based on the type of observations. They compared the results from their previous work (Lützgendorf et al. 2011), which was based on seeing-limited integrated light kinematics, and the results from Lanzoni et al. (2013) based on adaptive optics assisted resolved stellar kinematics in NGC 6388. They found that the integrated-light measurements can be biased towards higher velocities due to the contamination from bright stars close to the centre. On the other hand, resolved velocities can also be biased because the contamination from neighbouring stars can drive the individual star velocities to the mean velocity. We note that the previous observations from vdMA10 were using the *HST* proper motion data, whereas the studies from NGB08 and N10 were using the integrated-light data from GMOS-IFU and VLT-FLAMES, respectively. From our analyses, the velocity dispersions derived from discrete velocities are quite similar to the integrated-light measurements, and we do not find any notable difference in the measurements from resolved kinematics versus the integrated-light measurements (done by other work). This implies that the contamination effects are small while extracting our kinematics. Although the dispersion measurements are similar using different techniques, we note that the core density of ω Centauri is $\log\rho_c = 3.15$ M$_\odot$ pc^{-3} whereas NGC 6388 has a $\log\rho_c = 5.37$ M$_\odot$ pc^{-3} (Harris 1996), which is significantly denser. Due to this, although the contamination of light from neighbouring stars is higher for the integrated light measurements, the shot noise is much lower for NGC 6388 and is not affected by that uncertainty. For the MUSE data, we cannot make a straightforward comparison between the two clusters because of their different densities and different techniques involved in the extraction. Only a detailed analysis focusing on the differences between extraction techniques can help identify if there is a significant difference in the measurements obtained for ω Centauri and NGC 6388.

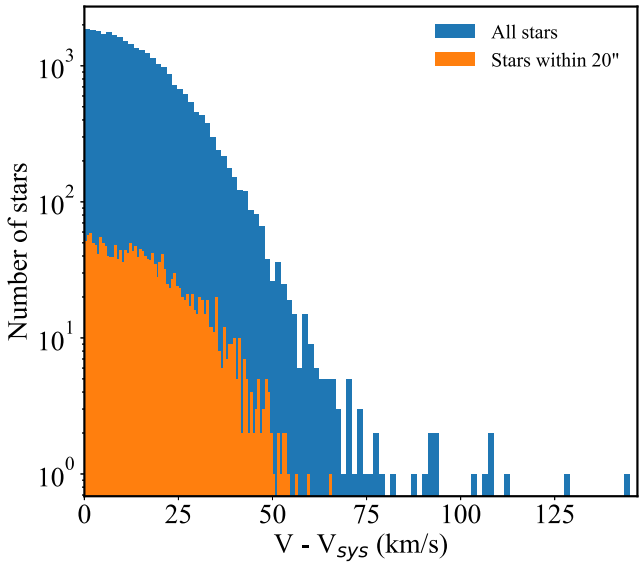

Figure 8. Histogram of the LOS velocities of all the stars with an S/N >8 excluding the foreground stars. Note that we have a few high-velocity stars but they are ∼1 arcmin away from the centre and none of them are close to the centre (within 20 arcsec).

6 HIGH-VELOCITY STARS IN ω CENTAURI

A smoking gun for the presence of an IMBH would be the detection of high-velocity stars close to the centre of ω Centauri using the NFM data. A discussion from Baumgardt et al. (2019) shows that for ω Centauri to host a 4.75 × 10^4 $M_\odot$ BH, a tail of at least 20 high–velocity stars >62 km s^{-1} should exist within 20 arcsec of the centre (see fig. 2 from Baumgardt et al. 2019). They ran a large grid of *N*-Body simulations that had several parameters such as the initial density profile, half-mass radius, the initial mass function, the cluster metallicity, and the mass fraction of an IMBH in the clusters. In addition, they varied the retention fraction of the stellar-mass BHs. The best-fitting model to the observed data had a 75 per cent retention fraction of stellar-mass BHs at the centre and no IMBH.

To test this theory, we looked for evidence of any high-velocity stars from our entire sample of stellar LOS velocities. We use an S/N cut of 8 but we do not use a cluster membership cut, since the membership estimation is also dependent on the LOS velocity of the stars. After the cut, we had 28 782 stars, out of which we excluded stars that were obvious non-members and foreground stars of MW with a mean velocity close to zero. For this, we removed stars with absolute velocities <75 km s^{-1}, which left us with a sample of 28 719 stars including members and non-members. We used our kinematic centre to estimate the distances for this analysis. We plot all these stars in Fig. 8. This contains 50 stars that have a velocity >62 km s^{-1}, but none are significant outliers within 20 arcsec (velocity and distance limits obtained from Baumgardt et al. (2019)). We define the significant outliers in the velocity higher than 62 km s^{-1} based on the uncertainty in the velocity of the star. A star would be a 1σ outlier if its velocity is higher than 62 km s^{-1} including its uncertainty at the 1σ level. From the histogram, we have 50 stars that have velocities >62 km s^{-1} out of which 22 are 1σ outliers, twelve are 2σ outliers and nine are 3σ outliers. We checked for the probability of the stars being binaries from a parallel work (Wragg et al. in preparation) and found that three out of those nine stars are likely binaries. From the six non-binary stars, we found one star that is at ∼20 arcsec with a velocity of 104 ± 1.5 km s^{-1}. We checked for the properties of this star on the CMD and it was redder than the main-sequence of the cluster, hence it is most likely a non-member of the cluster. This star also has a cluster membership probability of 0.0004 from our cluster membership analysis. The remaining stars are further away from the cluster centre (>1 arcmin). Their LOS velocities range from 92 to 128 km s^{-1}, and out of these, one star has a cluster membership probability of 0.99 and the rest of them are close to zero. A measure of the 3D velocities of these stars can indicate the nature of their high-velocities.

The above analysis from Baumgardt et al. (2019) was based on *N*-body simulations that were matched to the observed sample from Bellini et al. (2017). The Bellini et al. (2017) sample contained roughly 2900 stars within the central 20 arcsec. We have a similar number of stars (∼2500) compared to their sample within 20 arcsec, but note that they treat the two velocity components of the stars as separate measurements. Hence, the number of detected high-velocity stars in our sample should be halved (∼10). Although we do not detect any significant number of high-velocity stars as predicted from these simulations, there are still some possible implications to this: 1. There is no IMBH in ω Centauri. 2. The IMBH is smaller than ∼5 × 10^4 $M_\odot$. 3. The existing simulations might not be fully scaled to ω Centauri. From Baumgardt et al. (2019) simulations which were for a BH of ∼4.7 × 10^4 $M_\odot$, the number of high-velocity stars should scale with the BH mass. Assuming that the stars within the sphere of influence (SOI) are potentially high-velocity stars, the radius of the SOI scales with the BH mass, and the volume scales with the cube of the BH mass. Therefore, reducing the BH mass by 50 per cent results in a decrease in the number of high-velocity stars by a factor of 8, which in our case would be 5 stars for a BH mass of 2.3 × $10^4 M_\odot$. For a BH mass much lower than that, there might be no stars that we might be able to detect at all. This still does not completely rule out the no-IMBH scenario, and additional investigation using dynamical models is necessary.

7 SUMMARY AND DISCUSSION

In this paper, we used the MUSE WFM and NFM spectroscopic data to analyse the central kinematics of ω Centauri. The next paper in the series will present dynamical models based on different centres to infer whether a central dark mass or IMBH is present.

(i) We extracted the LOS velocities of 28 108 stars from both WFM and NFM data cubes. The data set is of the highest resolution yet obtained for the central 20 arcsec with a spatial resolution of 25 mas. We used the data to obtain the LOS velocity and velocity dispersion maps using KNN analysis and the LOESS method and then ran a *kinemetry* analysis on the maps. For the first time, our data set revealed that the central 20 arcsec of the cluster are counter-rotating with respect to the large-scale rotation that is on the scale of 100 arcsec, with a rotation speed of ∼3–4 km s^{-1}.

(ii) We used several methods to determine a kinematic centre for the cluster based on the counter-rotation and the peak in the velocity dispersion and finally used the kinemetry to constrain the centres using both kinematic maps. Our centre based on the counter-rotation was closest (∼5 arcsec) to the vdMA10 whereas the centre based on the dispersion peak was found to be near (∼2.5 arcsec) N10 centres. Both centres are offset by ∼10 arcsec, which is ∼0.25 pc.

(iii) We compared the proposed centres of ω Centauri from NGB08, N10, vdMA10, and our kinematic centre, and used those centres to derive the radial profiles for rotations and dispersions. We found similar trends in the dispersion profiles for different centres when compared to the previously observed data.

(iv) While comparing the dispersion profiles we also found that irrespective of whether the data was integrated-light kinematics or discrete velocities, the trends for the velocity dispersion profiles were similar.

(v) To search for evidence of any potential IMBH, we searched for high-velocity stars (>62 km s^{-1}) close to the centre (<20 arcsec) of the cluster but did not find any significant outliers. However, this does not completely rule out the IMBH as a lower mass in IMBH can result in non-detection of any high-velocity stars.

Assuming that the centre of ω Centauri contains an IMBH with a mass of 4.7 $\times$ 10^4 $M_\odot$, the sphere of influence is 15 arcsec, which is the region of the counter-rotation. An interesting possibility for the counter-rotation is the existence of a potential binary IMBH at the centre of the cluster. Simulations of 3-body encounters from Mapelli et al. (2005) show that a fraction of stars (55-70 per cent) tend to align their angular momentum to the binary IMBH. These simulations consist of 3-body encounters of two BHs (binary IMBH) and a cluster star of mass $0.5M_\odot$, where the trajectories of stars were observed that were scattered by the binary IMBH. If the binary BHs were massive enough and their orbits were wide enough and in addition, if their orbital angular momentum was higher than that of the incoming star, the star could co-rotate with its angular momentum aligned to the binary IMBH. In our case, if the binary IMBH orbital rotation is misaligned with the global rotation, there is a probability of finding stars aligned with the binary IMBH rotation and thus counter-rotating. But, this case is unlikely to explain the offset between the peak of the dispersion and the centre of the counter-rotation that we find. One scenario that can likely explain the offset in the counter-rotation and the dispersion peak is a wandering IMBH. de Vita, Trenti & MacLeod (2018) estimated a scaling relation between the cluster parameters and the wandering radius for an IMBH using *N*-body models. In particular, they derived the displacements of IMBHs in the clusters using a fixed ratio for cluster mass to IMBH mass and found that they deviated on average within 1 arcsec. But, they also found a few outliers, specifically for ω Centauri, which had an average displacement of 2.5 arcsec. Note that their assumptions relied on the extrapolations of BH mass scaling relationships, where they assumed a fixed mass ratio between $M_{BH}/M_{tot} = 10^3$. The lower mass end of the scaling relationships suffers from a significant scatter and thus the displacements can vary too. We used their equation (16) for a BH mass of 4.7 $\times$ $10^4 M_\odot$ to estimate a wandering radius r_w, which was ∼0.7 arcsec for a cluster core radius of 3.6 pc and mass of 3.6 $\times$ 10^6 $M_\odot$ (Baumgardt & Hilker 2018). The offset in our dispersion centre and the kinematic centre is ∼9 arcsec, and within 1σ this offset drops to ∼3 arcsec. A wandering IMBH explanation is not highly unlikely although more detailed simulations tailored to ω Centauri would be needed to investigate this scenario.

Several studies of early-type galaxies show a fraction of galaxies containing kinematically decoupled cores (KDCs) (e.g. Krajnović et al. 2011; Cappellari 2016). These are the cores of galaxies that are not aligned to the global rotation of the galaxy, which is usually a consequence of a previous merger (e.g. Kormendy et al. 1994; Hoffman et al. 2010). For example, the NSC of NGC 404 counter-rotates with respect to the galaxy(Seth et al. 2010; Nguyen et al. 2017), and this is believed to be due to a merger with a gas-rich dwarf around 1 Gyr ago. This is also supported by the young stars that are found near the centre of this galaxy. Many galaxies are also observed to show this behaviour such as NGC 4150, NGC 3032, NGC 4382, etc. (McDermid et al. 2006). Some GCs such as M15, which is a core-collapsed cluster (Usher et al. 2021), and M53 (Boberg et al. 2017) were also observed to have an inner rotation axis not aligned with the outer rotation similar to ω Centauri. If ω Centauri was formed through globular cluster mergers, there is a possibility for this kind of varied kinematics towards the centre. The half-mass relaxation time of ω Centauri is 9.6 Gyr (Harris 1996), so primordial kinematic features might still be observable. However, the relaxation time close to the centre will be much shorter, and thus an initial central counter-rotation should have been erased. Despite the general expectation that rotation is lost on relatively short time-scales, there is considerable nuclear rotation seen in many GCs with even shorter relaxation times than ω Centauri (e.g. Fabricius et al. 2014; Kamann et al. 2018). However, in a scenario with purely isotropic mergers of GCs, the expectation would probably be like in the case of galaxy dry mergers, a velocity field consistent with zero mean velocity and thus without any surviving rotating substructures (e.g. Hernquist 1993; Cox et al. 2006). But, recently Tsatsi et al. (2017) found that even pure isotropic GC mergers can result in a rotating NSC, but the mechanism is not trivial. ω Centauri also contains a complex population of stars and a spread in metallicities and ages (e.g. Johnson & Pilachowski 2010; Latour et al. 2021) that is suggestive of this scenario where different populations from multiple GCs might be surviving in the present-day cluster (e.g. Lee et al. 1999; Bedin et al. 2004).

Recently, data from Gaia was used to trace the origin of ω Centauri, where Majewski et al. (2012); Massari, Koppelman & Helmi (2019); Forbes (2020); Pfeffer et al. (2021) suggested it to be the former core of the *Gaia*-Enceladus/Sausage galaxy and galaxies are likely to contain central BHs. If there were strong tidal interactions in the past, then it is a possibility that the core along with its BH could have been offset from the global rotation. If the offset of the core is an imprint of this tidal interaction, this tidal effect must have acted along the north-south direction, e.g. when ω Centauri passed the Milky Way disk since we observe the counter-rotation elongated in that direction. These kinematics are indicative of a complex system with probable interactions in the past. However, recent studies by Tiongco, Vesperini & Varri (2018, 2022) used *N*-body simulations to follow the evolution of rotating star clusters in the presence of an external tidal field. They found that the dynamics within the cluster are perturbed by the tidal field, mainly a tidal torque from the host galaxy that affects the internal rotation of the cluster and introduces a precession of the cluster's rotation axis. Mostly, the inner regions are dominated by the cluster's natal rotation, which is dependent on the initial conditions, whereas precession is introduced in the outer parts of the cluster. As the cluster evolves, a radial variation of the rotation axis is observed, and depending on the initial intrinsic rotation, it can lead to a counter-rotation in the cluster. When compared, the precession would have to be observed in the outer parts of the cluster that are beyond the half-mass radius of the cluster (10.4 pc), whereas we observe the counter-rotation within the central 20 arcsec (0.5 pc). It is highly unlikely from these simulations that the counter-rotation was caused by tidal effects.

Our next step is to model the kinematics using Schwarzschild dynamical models. This will allow us to constrain a possible IMBH or dark remnant mass distribution in this cluster. It is challenging, however, to set up this model due to the counter-rotation, its offset from the dispersion peak, and overall, the outer kinematics may dominate the rotation field.

ACKNOWLEDGEMENTS

RP and SK acknowledge funding from UKRI in the form of a Future Leaders Fellowship (grant no. MR/T022868/1). PMW acknowledges support by the BMBF from the ErUM program (project VLT-BlueMUSE, grant no. 05A20BAB).

Based on observations collected at the European Organisation for Astronomical Research in the Southern Hemisphere under ESO programs 0103.D-0204, 0104.D-0257, 105.20CR, and 109.23DV.

DATA AVAILABILITY

The data underlying this paper will be shared on reasonable request to the corresponding author.

REFERENCES

Ahn C. P. et al., 2017, ApJ, 839, 72
Ahn C. P. et al., 2018, ApJ, 858, 102
Alfaro-Cuello M. et al., 2019, ApJ, 886, 57
Anderson J., van der Marel R. P., 2010, ApJ, 710, 1032
Anderson J. et al., 2008, AJ, 135, 2055
Baumgardt H., 2017, MNRAS, 464, 2174
Baumgardt H., Hilker M., 2018, MNRAS, 478, 1520
Baumgardt H., Makino J., Hut P., 2005, ApJ, 620, 238
Baumgardt H. et al., 2019, MNRAS, 488, 5340
Bedin L. R., Piotto G., Anderson J., Cassisi S., King I. R., Momany Y., Carraro G., 2004, ApJ, 605, L125
Beers T. C., Flynn K., Gebhardt K., 1990, AJ, 100, 32
Bellini A., Anderson J., Bedin L. R., King I. R., van der Marel R. P., Piotto G., Cool A., 2017, ApJ, 842, 6
Bianchini P., van der Marel R. P., del Pino A., Watkins L. L., Bellini A., Fardal M. A., Libralato M., Sills A., 2018, MNRAS, 481, 2125
Boberg O. M., Vesperini E., Friel E. D., Tiongco M. A., Varri A. L., 2017, ApJ, 841, 114
Bressan A., Marigo P., Girardi L., Salasnich B., Dal Cero C., Rubele S., Nanni A., 2012, MNRAS, 427, 127
Brown A. M., Massey R., Lacroix T., Strigari L. E., Fattahi A., Bœhm C., 2019, preprint (arXiv:1907.08564)
Cappellari M., 2016, ARA&A, 54, 597
Cappellari M. et al., 2013, MNRAS, 432, 1862
Cleveland W. S., 1979, J. Am. Stat. Assoc., 74, 829
Cleveland W. S., Devlin S. J., 1988, J. Am. Stat. Assoc., 83, 596
Cox T. J., Dutta S. N., Di Matteo T., Hernquist L., Hopkins P. F., Robertson B., Springel V., 2006, ApJ, 650, 791
de Vita R., Trenti M., MacLeod M., 2018, MNRAS, 475, 1574
Evans A. J., Strigari L. E., Zivick P., 2022, MNRAS, 511, 4251
Fabricius M. H. et al., 2014, ApJ, 787, L26
Fétick R. J. L. et al., 2019, A&A, 628, A99
Fiestas J., Spurzem R., Kim E., 2006, MNRAS, 373, 677
Forbes D. A., 2020, MNRAS, 493, 847
Foreman-Mackey D., Hogg D. W., Lang D., Goodman J., 2013, PASP, 125, 306
Freeman K. C., Rodgers A. W., 1975, ApJ, 201, L71
Fusco T. et al., 2020, A&A, 635, A208
Gebhardt K., Rich R. M., Ho L. C., 2005, ApJ, 634, 1093
Geyer E. H., Hopp U., Nelles B., 1983, A&A, 125, 359
Giesers B. et al., 2019, A&A, 632, A3
Göttgens F. et al., 2021, MNRAS, 507, 4788
Gratton R. G., Carretta E., Bragaglia A., 2012, A&A Rev., 20, 50
Greene J. E., Strader J., Ho L. C., 2020, ARA&A, 58, 257
Habouzit M. et al., 2021, MNRAS, 503, 1940
Harris W. E., 1996, AJ, 112, 1487
Helmi A., Babusiaux C., Koppelman H. H., Massari D., Veljanoski J., Brown A. G. A., 2018, Nature, 563, 85
Hernquist L., 1993, ApJ, 409, 548
Hoffman L., Cox T. J., Dutta S., Hernquist L., 2010, ApJ, 723, 818
Husser T. O., Wende-von Berg S., Dreizler S., Homeier D., Reiners A., Barman T., Hauschildt P. H., 2013, A&A, 553, A6
Husser T.-O. et al., 2016, A&A, 588, A148
Husser T.-O. et al., 2020, A&A, 635, A114
Ibata R. et al., 2009, ApJ, 699, L169
Jedrzejewski R. I., 1987, MNRAS, 226, 747
Johnson C. I., Pilachowski C. A., 2010, ApJ, 722, 1373
Kamann S., 2018, PampelMuse: Crowded-field 3D spectroscopy, recor-dascl:1805.021
Kamann S., Wisotzki L., Roth M. M., 2013, A&A, 549, A71
Kamann S. et al., 2016, A&A, 588, A149
Kamann S. et al., 2018, MNRAS, 473, 5591
Kelly B. C., 2007, ApJ, 665, 1489
Kormendy J., Dressler A., Byun Y. I., Faber S. M., Grillmair C., Lauer T. R., Richstone D., Tremaine S., 1994, in European Southern Observatory Conference and Workshop Proceedings, ESOC, 49, 147K. p. 147
Krajnović D., Cappellari M., de Zeeuw P. T., Copin Y., 2006, MNRAS, 366, 787
Krajnović D. et al., 2008, MNRAS, 390, 93
Krajnović D. et al., 2011, MNRAS, 414, 2923
Kruijssen J. M. D., Portegies Zwart S. F., 2009, ApJ, 698, L158
Lanzoni B. et al., 2013, ApJ, 769, 107
Latour M., Calamida A., Husser T. O., Kamann S., Dreizler S., Brinchmann J., 2021, A&A, 653, L8
Leaman R., 2012, AJ, 144, 183
Lee Y. W., Joo J. M., Sohn Y. J., Rey S. C., Lee H. C., Walker A. R., 1999, Nature, 402, 55
Lee Y. W., Rey S. C., Ree C. H., Joo J. M., Sohn Y. J., Yoon S. J., 2002, in van Leeuwen F., Hughes J. D., Piotto G.eds, ASP Conf. Ser.Vol. 265, Omega Centauri, a Unique Window into Astrophysics. Astron. Soc. Pac., San Francisco, p. 305
Lützgendorf N., Kissler-Patig M., Noyola E., Jalali B., de Zeeuw P. T., Gebhardt K., Baumgardt H., 2011, A&A, 533, A36
Lützgendorf N., Gebhardt K., Baumgardt H., Noyola E., Neumayer N., Kissler-Patig M., de Zeeuw T., 2015, A&A, 581, A1
Lynden-Bell D., 1967, MNRAS, 136, 101
Majewski S. R., Nidever D. L., Smith V. V., Damke G. J., Kunkel W. E., Patterson R. J., Bizyaev D., García Pérez A. E., 2012, ApJ, 747, L37
Mapelli M., Colpi M., Possenti A., Sigurdsson S., 2005, MNRAS, 364, 1315
Martocchia S. et al., 2018, MNRAS, 473, 2688
Massari D., Koppelman H. H., Helmi A., 2019, A&A, 630, L4
Mayor M. et al., 1997, AJ, 114, 1087
McDermid R. M. et al., 2006, MNRAS, 373, 906
Merritt D., Meylan G., Mayor M., 1997, AJ, 114, 1074
Meylan G., Mayor M., 1986, A&A, 166, 122
Meylan G., Mayor M., Duquennoy A., Dubath P., 1995, A&A, 303, 761
Nguyen D. D. et al., 2017, ApJ, 836, 237
Nguyen D. D. et al., 2018, ApJ, 858, 118
Nguyen D. D. et al., 2019, ApJ, 872, 104
Nitschai M. S. et al., 2023, ApJ, 958, 8
Noyola E., Gebhardt K., Bergmann M., 2008, ApJ, 676, 1008
Noyola E., Gebhardt K., Kissler-Patig M., Lützgendorf N., Jalali B., de Zeeuw P. T., Baumgardt H., 2010, ApJ, 719, L60
Pechetti R. et al., 2022, ApJ, 924, 48
Pedregosa F. et al., 2011, J. Mach. Learn. Res., 12, 2825
Pfeffer J., Lardo C., Bastian N., Saracino S., Kamann S., 2021, MNRAS, 500, 2514
Piotto G. et al., 2015, AJ, 149, 91
Pryor C., Meylan G., 1993, in Djorgovski S. G., Meylan G.eds, ASP Conf. Ser. Vol. 50, Structure and Dynamics of Globular Clusters. Astron. Soc. Pac., San Francisco, 1993ASPC, p. 357
Reijns R. A., Seitzer P., Arnold R., Freeman K. C., Ingerson T., van den Bosch R. C. E., van de Ven G., de Zeeuw P. T., 2006, A&A, 445, 503
Robin A. C., Reylé C., Derrière S., Picaud S., 2003, A&A, 409, 523
Saglia R. P. et al., 2016, ApJ, 818, 47
Sarajedini A. et al., 2007, AJ, 133, 1658
Seth A. C. et al., 2010, ApJ, 714, 713
Seth A. C. et al., 2014, Nature, 513, 398
Sollima A., Baumgardt H., Hilker M., 2019, MNRAS, 485, 1460
Suntzeff N. B., Kraft R. P., 1996, AJ, 111, 1913
Tiongco M. A., Vesperini E., Varri A. L., 2018, MNRAS, 475, L86

Tiongco M. A., Vesperini E., Varri A. L., 2022, MNRAS, 512, 1584
Tsatsi A., Mastrobuono-Battisti A., van de Ven G., Perets H. B., Bianchini P., Neumayer N., 2017, MNRAS, 464, 3720
Usher C., Kamann S., Gieles M., Hénault-Brunet V., Dalessandro E., Balbinot E., Sollima A., 2021, MNRAS, 503, 1680
van de Ven G., van den Bosch R. C. E., Verolme E. K., de Zeeuw P. T., 2006, A&A, 445, 513
van der Marel R. P., Anderson J., 2010, ApJ, 710, 1063
van Leeuwen F., Le Poole R. S., Reijns R. A., Freeman K. C., de Zeeuw P. T., 2000, A&A, 360, 472
Volonteri M., 2010, A&AR, 18, 279
Walker M. G., Mateo M., Olszewski E. W., Sen B., Woodroofe M., 2009, AJ, 137, 3109
Weilbacher P. M. et al., 2020, A&A, 641, A28
Zocchi A., Gieles M., Hénault-Brunet V., 2019, MNRAS, 482, 4713

APPENDIX A:

KNN-velocity dispersion maps

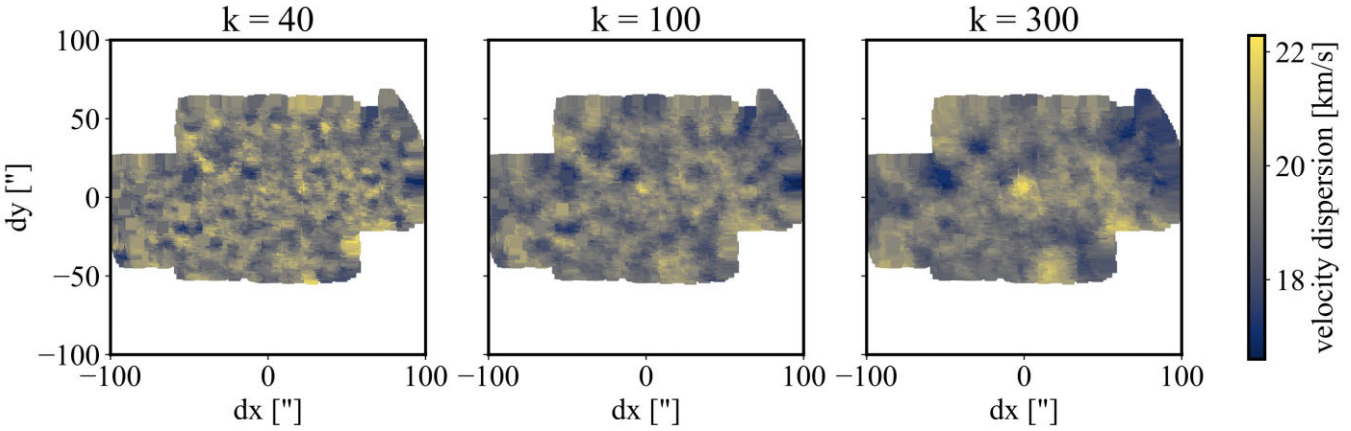

Figure A1. Velocity dispersion maps of ω Centauri. The maps describe the velocity dispersion determined using the k-nearest neighbours method. From left to right: the k-value increases from 40 to 300 in the KNN analysis. A central peak is visible for the k-value of 300. This peak coincides with the centre from N10 since their centre was derived based on the peak of the velocity dispersion.

This paper has been typeset from a TEX/LATEX file prepared by the author.